

Article

# Construction of Hexagonal Prism-like Defective BiOCl Hierarchy for Photocatalytic Degradation of Tetracycline Hydrochloride

Lijun Hu<sup>1,2,\*</sup> , Zhichao Ding<sup>1,2</sup>, Fei Yan<sup>1,2</sup>, Kuan Li<sup>1,2</sup>, Li Feng<sup>3</sup> and Hongqing Wang<sup>1,2,\*</sup><sup>1</sup> School of Chemistry and Chemical Engineering, University of South China, Hengyang 421001, China<sup>2</sup> Hunan Key Laboratory for the Design and Application of Actinide Complexes, University of South China, Hengyang 421001, China<sup>3</sup> School of Civil and Transportation Engineering, Guangdong University of Technology, Guangzhou 510006, China

\* Correspondence: lijun.hu@usc.edu.cn (L.H.); hqwang@usc.edu.cn (H.W.)

**Abstract:** Oxygen vacancy manipulation and hierarchical morphology construction in oxygen-containing semiconductors have been demonstrated to be effective strategies for developing high efficiency photocatalysts. In most studies of bismuth-based photocatalysts, hierarchical morphology and crystal defects are achieved separately, so the catalysts are not able to benefit from both features. Herein, using boiling ethylene glycol as the treatment solution, we developed an etching-recrystallization method for the fabrication of 3D hierarchical defective BiOCl at ambient pressure. The target hierarchical 3D-BiOCl is composed of self-assembled BiOCl nanosheets, which exhibit a hexagonal prism-like morphology on a micron scale, while simultaneously containing numerous oxygen vacancies within the crystal structure. Consequently, the target catalyst was endowed with a higher specific surface area, greater light harvesting capability, as well as more efficient separation and transfer of photo-excited charges than pristine BiOCl. As a result, 3D-BiOCl presented an impressive photocatalytic activity for the degradation of tetracycline hydrochloride in both visible light and natural white light emitting diode (LED) irradiation. Moreover, an extraordinary recycling property was demonstrated for the target photocatalyst thanks to its hierarchical structure. This study outlines a simple and energy-efficient approach for producing high-performance hierarchically defective BiOCl, which may also open up new possibilities for the morphological and crystal structural defect regulation of other Bi-based photocatalysts.

**Keywords:** BiOCl; photocatalytic; lattice defects; hierarchical structure; degradation; ambient pressure



**Citation:** Hu, L.; Ding, Z.; Yan, F.; Li, K.; Feng, L.; Wang, H. Construction of Hexagonal Prism-like Defective BiOCl Hierarchy for Photocatalytic Degradation of Tetracycline Hydrochloride. *Nanomaterials* **2022**, *12*, 2700. <https://doi.org/10.3390/nano12152700>

Academic Editors: Giuseppe Cappelletti, Jinhong Bi and Guocheng Huang

Received: 14 July 2022

Accepted: 1 August 2022

Published: 5 August 2022

**Publisher's Note:** MDPI stays neutral with regard to jurisdictional claims in published maps and institutional affiliations.



**Copyright:** © 2022 by the authors. Licensee MDPI, Basel, Switzerland. This article is an open access article distributed under the terms and conditions of the Creative Commons Attribution (CC BY) license (<https://creativecommons.org/licenses/by/4.0/>).

## 1. Introduction

Advanced oxidation processes of semiconductor photocatalysis have been deemed a viable strategy for removing toxic and poisonous compounds owing to their low energy consumption and environmental protection features [1–3]. Researchers have exploited a variety of efficient photocatalysts in the past to cover the demands, including TiO<sub>2</sub>, ZnO, CeO<sub>2</sub>, CdS, and C<sub>3</sub>N<sub>4</sub> [4–9]. Among these, bismuth oxychloride (BiOCl) has emerged as one of the most promising photocatalysts in recent years owing to its unique layered structure [Cl–O–Bi–O–Cl] and elastic optoelectronic properties [10–12]. It has been thoroughly demonstrated over the past years that the self-constructed internal electric field along the direction of [001] is capable of greatly facilitating electron–hole pair separation, allowing the possibility for BiOCl to achieve high quantum efficiency levels. Moreover, the low bond energy and long bond length of the Bi–O bonds in BiOCl enable the development of deficient photocatalysts more easily than traditional catalysts. Up to now, considerable development has been made in the field of BiOCl photocatalysts, which have

been successfully applied in photocatalytic hydrogen and oxygen production, pollutant degradation, nitrogen fixation, carbon dioxide reduction, selective organic transformation, and other applications [9,13–15]. Yet, despite this, the broad band gap energy of BiOCl (3.27 eV) and the high rate of charge recombination under solar light limit its efficiency as a photocatalyst [16,17].

To meet the aforementioned challenge, numerous strategies have been proposed for extending the light absorption range and suppressing carrier recombination of BiOCl photocatalysts, such as doping, loading a noble metal, modifying the morphology, or combining with other photocatalysts [17–21]. Modifications involving morphological engineering have been shown to be effective for enhancing photocatalytic activity. In a study by Huang et al., for example, in situ topotactic transformation of BiVO<sub>4</sub> was used to obtain ultrathin BiOCl nanosheets, which increased the specific surface area of specimens and ciprofloxacin degradation efficiency compared with the bulk BiOCl [22]. Using a wet chemical approach, Zhang and co-workers constructed BiOCl nanosheets with periodic nano-channels, which presented a longer lifetime of excitons than the control sample [23]. In consequence, the target photocatalyst outperformed the control specimens in photo-oxidation of benzylamine coupling by a factor of 30. As well as controlling the morphology, generating oxygen vacancies (OVs) in the crystal structure is an efficient means for improving the photocatalysis efficiency of specimens. On one side, OVs can create defective energy levels in the forbidden band, thus extending the photo-absorption range [24–27]. The OVs on the surface of the photocatalyst, on the other hand, can serve as reactive sites for the absorption and activation of reactive species [9,28]. However, in most studies of bismuth-based photocatalysts, hierarchical morphology and crystal defects are achieved separately, so the catalysts are not able to benefit from both features. Therefore, it is particularly appealing to endow a specific hierarchical shape and lattice defect simultaneously in the BiOCl photocatalyst to expose more reaction sites and enhance charge transfer efficiency during the photocatalytic process.

In this work, we develop a simple etching-recrystallization process at ambient pressure for obtaining a three-dimensional hierarchical defect BiOCl photocatalyst (abbreviated as 3D-BiOCl). The results of the study indicate that 3D-BiOCl constructed in boiling ethylene glycol (EG) exhibits oxygen vacancies in abundance and a hierarchical hexagonal morphology at the micron level. Such features enhance its specific surface area, solar light absorption, as well as the separation and transfer of photo-excited charges. As a consequence, the target 3D-BiOCl photocatalyst exhibits significantly greater tetracycline hydrochloride degradation efficiency under visible and natural white LED light than pristine BiOCl. Furthermore, owing to the hierarchical structure of the target photocatalyst, it demonstrates excellent recycling potential as well. Our findings, we believe, may also provide insight into the morphological and crystal structural defects regulation of other Bi-based photocatalysts.

## 2. Experimental

### 2.1. Materials

Bismuth trioxide (Bi<sub>2</sub>O<sub>3</sub>, AR), ethanol (C<sub>2</sub>H<sub>6</sub>O, 99.7% purity), ethylene glycol (EG, AR, 99% purity), and tetracycline hydrochloride (C<sub>22</sub>H<sub>24</sub>N<sub>2</sub>O<sub>8</sub>·HCl, 96% purity) were purchased from Aladdin Reagents Co., Ltd. (Shanghai, China), and all the chemical reagents were used as received without further treatment or purification.

### 2.2. Preparation of Pristine BiOCl Nanosheets

The BiOCl nanosheets, according to previous work, were prepared using a modified hydrothermal method. The typical process for synthesizing BiOCl nanosheets starts with 0.968 g (2 mmol) bismuth nitrate pentahydrate (Bi(NO<sub>3</sub>)<sub>3</sub>·5H<sub>2</sub>O) being poured into 50 mL ultrapure water and vigorously stirred [29]. Afterward, 10 mL of saturated sodium chloride (NaCl) was added to the above solution to form a white suspension. After the mixture was processed, it was placed in a Teflon-lined stainless steel autoclave and maintained at 160 °C

for three hours. As soon as the reactor cools to ambient temperature, the white product BiOCl is centrifuged and rinsed with ultrapure water and ethanol five times before being dried at 100 °C for 12 h.

### 2.3. Preparation of 3D-BiOCl Photocatalyst

In this study, 3D-BiOCl was received by etching pristine BiOCl and re-crystallizing it at atmospheric pressure. In detail, 30 mL of ethylene glycol was first added to a 100 mL flat bottom beaker and boil on a hotplate. Following this, 0.5 g of pristine BiOCl powder was added directly to the boiling solution and etched for 30 min to construct the target photocatalyst. Finally, the 3D-BiOCl photocatalyst was collected following centrifugation, rinsed with ultra-pure water and ethanol four times, and then dried for 12 h at 100 °C in a vacuum oven.

### 2.4. Characterization

X-ray diffraction (XRD) patterns were recorded using a PANalytical Empyrean diffractometer (PANalytical, Almelo, the Netherlands) with Cu K $\alpha$  radiation ( $\lambda = 1.5406 \text{ \AA}$ ). Scanning electron microscopy (SEM) and energy dispersive spectroscopy (EDS) images were recorded by a field emission scanning electron microscope (JSM-7800F, JEOL Ltd., Tokyo, Japan). The steady-state photoluminescence (PL) spectra were collected using a fluorescence spectrophotometer (Cary Eclipse, Agilent, Santa Clara, CA, USA) with an excitation wavelength of 300 nm. Raman spectra were obtained using a confocal Raman Microscope LabRAM HR Evolution (HORIBA, London, UK) equipped with a laser emitting at 514 nm. X-ray photoelectron spectroscopy (XPS) data were acquired in the Thermo Scientific K-Alpha XPS spectrometer (Thermo Fisher Scientific Inc., Waltham, MA, USA). A CHI660E electrochemical workstation with a three-electrode cell was used to measure the electrochemical impedance spectroscopy (EIS) and photocurrent. The optical absorption and nitrogen adsorption–desorption isotherms of photocatalysts were collected on UV-3600 UV/Vis diffuse reflectance spectrophotometer (Shimadzu, Tokyo, Japan) and Micromeritics ASAP 2460 Surface Area and Porosity Analyzer (Micromeritics ASAP 2460, Norcross, GA, USA), respectively. On a Bruker EMX Plus spectrometer (Karlsruhe, Germany), electron paramagnetic resonance (EPR) spectra were collected.

### 2.5. Photocatalytic Measurements

The photocatalytic activities of BiOCl and 3D-BiOCl were evaluated by degradation of tetracycline hydrochloride (TC-HCl) under visible light and LED light. For LED light and visible light, a 55 W 4000K LED light (YMZB-GDZN, Zhongshan, China YAME) and a 300 W xenon lamp with a 420 nm filter (HSX-F300, Beijing NBet), respectively, were employed. In a typical photocatalytic process, 100 mg of photocatalyst is dispersed into 100 mL of 30 mg/L TC-HCl solution in a 250 mL cylindrical glass reactor, followed by magnetic stirring for 60 min under darkness to establish an adsorption–desorption equilibrium. After that, the reaction cell was transferred to a distance of about 30 cm from the light source to perform photocatalytic degradation of TC-HCl. During the photocatalytic process, 2 mL dispersion was sucked out to measure the concentration of TC-HCl solution by UV/Vis spectrophotometer every 10 min ( $\lambda = 358 \text{ nm}$ ). Figure S1 depicts the UV/Vis absorbance spectrum of TC-HCl, which exhibits an obvious characterized absorption peak at 358 nm.

## 3. Results and Discussion

### 3.1. Morphology and Structure of Photocatalysts

In this study, a 3D-BiOCl photocatalyst was prepared by etching BiOCl nanosheets in boiling EG followed by recrystallization of the etching products, as indicated schematically in Figure 1. The morphologies and component distribution of the BiOCl and 3D-BiOCl were first visualized by SEM with EDS. According to Figure S2, the bulk BiOCl product obtained by hydrothermal preparation was composed of numerous nanoplates with an average size of around 800 nm. Compared with the typical lamellar morphology of pristine

BiOCl, the as-obtained 3D BiOCl sample exhibited a striking hexagonal prism structure, with a length of up to tens of micrometers, as exhibited in Figure 1a,b and Figure S3. It is interesting to note that a high-magnification SEM image in Figure 1c clearly demonstrates that the 3D-BiOCl hexagonal prism was assembled by small nanoplates with a width within a few tens of nanometers. Such a hierarchical structure can effectively prevent the stacking of nanosheets, resulting in a high surface area and excellent recyclability for photocatalysts [30,31].

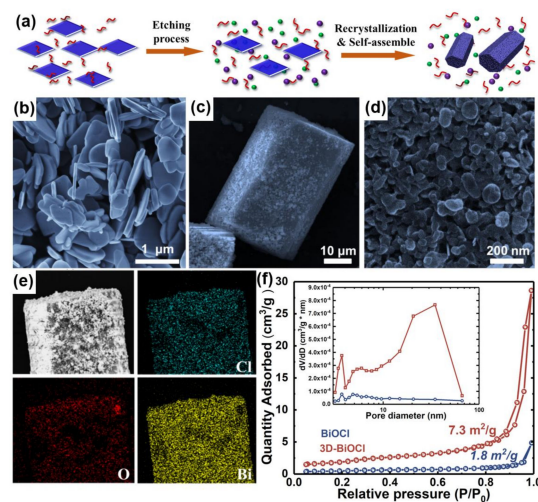


**Figure 1.** (a) Schematic illustration of the 3D-BiOCl fabrication process; SEM pictures of 3D-BiOCl (b–d); (e) Cl, O, and Bi element mappings of 3D-BiOCl specimen; and (f)  $N_2$  adsorption–desorption isotherms and pore size distributions (inset) of BiOCl and 3D-BiOCl.

To further confirm the 3D hierarchical structure of re-crystallized specimens, nitrogen adsorption–desorption isotherms were carefully measured at 77 K. As depicted in Figure 1f, the Brunauer Emmett Teller (BET) surface area of the pristine BiOCl was only  $1.8 \text{ m}^2 \cdot \text{g}^{-1}$ , which is in line with previous work. Fascinatingly, an even higher specific surface area ( $7.3 \text{ m}^2 \cdot \text{g}^{-1}$ ) and a larger mesoporous volume were characterized in 3D-BiOCl, which indicates that the hierarchical structure of microns 3D-BiOCl is not limited to the surface, but is present throughout the whole structure. Furthermore, the hysteresis loop in the range of  $0.8\text{--}1.0 P/P_0$  as well as the distribution of pore sizes is also indicative of a mesoporous structure characteristic of 3D-BiOCl. The distributions of the elements in 3D-BiOCl were mapped utilizing the EDS mapping technology developed by SEM, as shown in Figure 1e. As can be seen, Bi, Cl, and O elements are distributed homogeneously throughout the target sample, and no impurities have been detected. Based on the results of the foregoing studies, it can be concluded that, by re-crystallizing pure BiOCl in boiling EG, a hexagonal prism-like 3D hierarchical BiOCl was formed.

Upon recognizing the significant morphological difference between BiOCl and 3D-BiOCl, X-ray diffraction (XRD) patterns with a  $2\theta$  range of  $10\text{--}60^\circ$  were collected to explore the influence of the recrystallization process on the phase composition and crystallographic structure. Figure 2a shows that all of the diffraction peaks are completely indexed to a tetragonal structure typical for BiOCl (JCPDS No.85–0861), with no traces of impurities, thereby indicating both specimens are composed entirely of pure BiOCl [32,33]. In contrast to the identical phase composition, 3D-BiOCl displayed a widening of the diffraction peaks over pure BiOCl, indicating that the re-crystallized sample had a smaller crystal size, which is consistent with observations of SEM. Moreover, differences are more exposed when the details of diffraction peaks are analyzed, as presented in Figure 2b,c. Compared with pristine BiOCl, a distinct shift in diffraction peaks occurs in 3D BiOCl, in which the (001) and (012) peaks shift to a smaller diffraction angle, whereas the (110) peak shifts to a larger diffraction angle. The shift of (001), (012), and (110) peaks is about  $0.06^\circ$ ,  $0.03^\circ$ , and  $0.07^\circ$ , respectively, in excess of the instrument bias of about  $0.02^\circ$ , suggesting an anisotropic

distortion in the 3D-BiOCl crystal lattice, which is typically caused by lattice defects, such as substitutions and vacancies in the crystal [34–36].

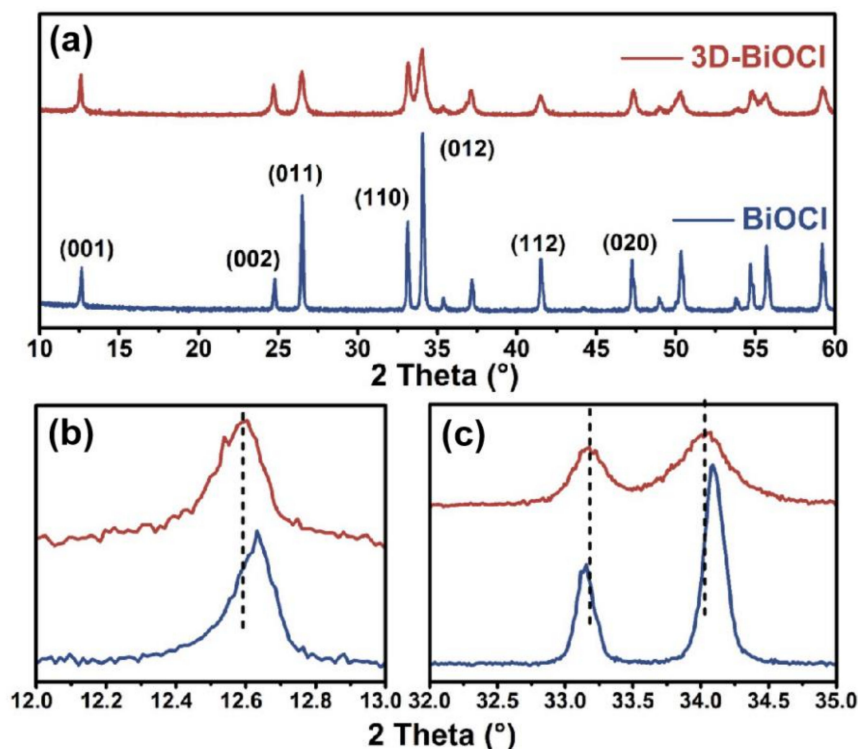


**Figure 2.** (a) XRD diffraction patterns of BiOCl (blue) and 3D-BiOCl (red); (b,c) zoomed-in images of XRD spectra in the range of 12–13° and 32–35°, respectively.

Re-crystallization of BiOCl resulted in micro-structural changes and shifted diffraction peaks, which were further investigated using Raman and electron paramagnetic resonance (EPR). Figure 3a provides the representative Raman spectroscopic results of as-prepared samples in the range of 50–450  $\text{cm}^{-1}$ . Four characteristic vibration bands were detected in virgin BiOCl at 397.8, 199.4, 143.3, and 58.4  $\text{cm}^{-1}$ , which are consistent with the majority of prior studies on BiOCl. Specifically, the peak at 397.8  $\text{cm}^{-1}$  corresponds to the  $B_{1g}$  and  $E_g$  of the motorial oxygen atoms; the peak at 199.2  $\text{cm}^{-1}$  is allocated to the  $A_{1g}$  internal stretching modes of Bi-Cl; and the peaks at 58.4  $\text{cm}^{-1}$  and 143.3  $\text{cm}^{-1}$  pertain to  $A_{1g}$  external and internal stretching modes of Bi-Cl, respectively [35,37]. When comparing 3D-BiOCl to BiOCl, three major differences in the spectrum were identified, including a blue-shift in the vibration peak, broadening of peaks, and the creation of a new peak at 95  $\text{cm}^{-1}$ . The newly discovered vibration band at 95  $\text{cm}^{-1}$  is produced from the  $E_g$  and  $A_{1g}$  vibration modes of Bi metal, revealing that 3D-BiOCl contains crystal defects as well as trace amounts of reduced Bi [38]. Additionally, the vibration band broadening and position shifting may be related to the novel shape and oxygen vacancy of the 3D-BiOCl sample [39,40]. A similar phenomenon was also observed in ultra-thin and defective BiOCl [41]. As an effective approach for probing electrons trapped in oxygen vacancies, EPR was adopted to obtain more intuitive evidence for oxygen vacancies in 3D-BiOCl. When compared with pristine BiOCl, the EPR results of 3D-BiOCl demonstrate a distinct signal at  $g = 2.003$  attributed to the oxygen vacancy trapped electrons, as seen in Figure 3b. This finding further shows that, during the re-crystallization process, oxygen vacancies were introduced into the crystal structure of BiOCl.

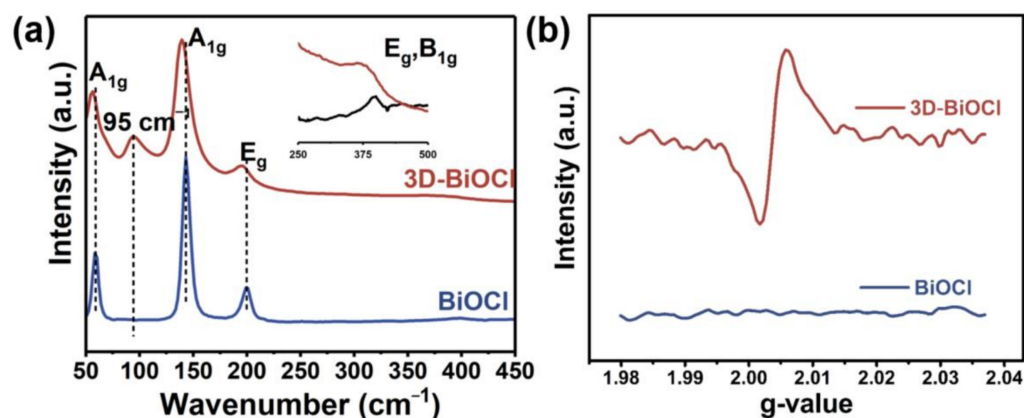
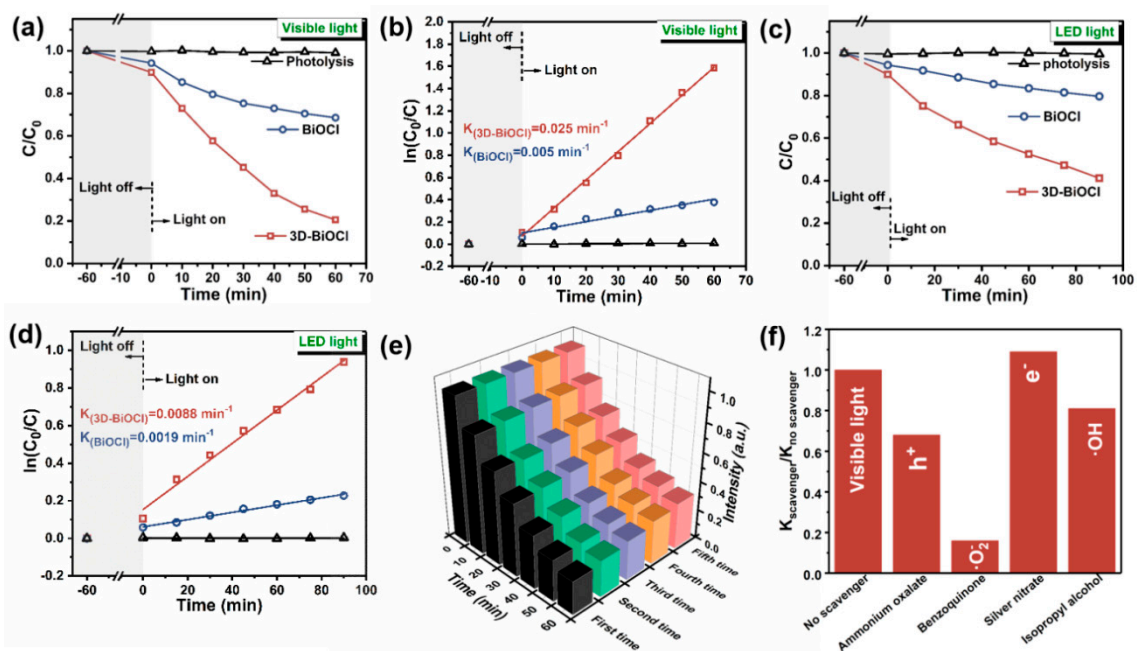


Figure 3. (a) Raman and (b) EPR spectra of BiOCl and 3D-BiOCl specimens.

### 3.2. Photocatalytic Activity and Stability of Photocatalysts under Visible Light

To disclose the role of the hierarchical structure and oxygen vacancy of 3D BiOCl in affecting photocatalysis, tetracycline hydrochloride (TC-HCl) was selected as a target contaminant to evaluate the photocatalytic activity and stability of as-obtained samples. Figure 4a depicts a representative temporal evolution curve of the relative concentration of TC-HCl solution with or without a photocatalyst. Before being exposed to visible light, the solution was vigorously stirred in the dark for 60 min to achieve adsorption–desorption equilibrium, and the quantity of TC-HCl uptake by the BiOCl samples was determined using the equation  $q(\text{TC} - \text{HCl}) = (V * dC) / m(\text{BiOCl})$ . In agreement with the surface area of specimens, the obtained adsorption quantity of 3D-BiOCl is  $3.3 \text{ mg} \cdot \text{g}^{-1}$ , which is larger than the  $1.8 \text{ mg} \cdot \text{g}^{-1}$  of BiOCl. Upon exposure to visible light for one hour, the self-photo-degradation of TC-HCl is almost negligible, indicating its excellent photostability. In contrast, using BiOCl and 3D-BiOCl as photocatalysts, an apparent degradation of tetracycline was observed. In contrast, when 3D-BiOCl or BiOCl photocatalyst was added to the reaction, tetracycline was degraded. Using 3D-BiOCl as the photocatalyst, 80 percent of tetracycline was degraded within one hour of exposure to visible light in comparison with merely 31 percent for BiOCl in the same execution environment, suggesting superior photocatalytic degradation ability for 3D-BiOCl. Moreover, the TC-HCl degradation results were subjected to kinetic fitting in order to quantitatively compare the catalytic rates of the samples. As shown in Figure 4b, the degradation curves of both specimens could be well described by the pseudo-first-order kinetics model, and the degradation rates of BiOCl and 3D-BiOCl extracted from the linear fitting between  $\ln(C/C_0)$  and time were  $0.005$  and  $0.025 \text{ min}^{-1}$ , respectively. It is worth noting that 3D-BiOCl exhibits higher photocatalytic degradation activity with visible light than most other photocatalysts, especially for Bi-based photocatalysts (Table 1). Further, BiOCl pearlescent powder is a potential home decorative material thanks to its non-toxic and environmentally friendly properties. Therefore, it is critical that this material exhibits photocatalytic activity in an interior setting. For this purpose, a natural white LED with 4000 K bulbs was used as the light source to assess the TC-HCl photo-degradation capacities of samples in a home environment. According to Figure 4c, after 90 min of LED illumination, 21 and 59 percent of tetracycline were degraded using BiOCl and 3D-BiOCl as photocatalysts, with corresponding degradation rates of  $0.0019$  and  $0.0088 \text{ min}^{-1}$ , respectively. Thus, it can be concluded that 3D-BiOCl fabricated by re-crystallization of the original BiOCl is more photo-catalytically active under both visible and natural white (LED) light.



**Figure 4.** Photocatalytic tetracycline hydrochloride (TC-HCl) degradation under visible light (a), natural white LED (c), and (b,d) corresponding pseudo-first-order kinetic fitting curves; (e) cycle studies on TC-HCl degradation by 3D-BiOCl under visible light; (f) photocatalytic removal of TC-HCl in the presence of different scavengers by 3D-BiOCl under visible light.

**Table 1.** Comparison of the degradation kinetic constants of TC for various photocatalysts.

Types of Photocatalyst	Light Source	Concentration of TC-HCl (mg/L)	Photocatalyst Dosage (g/L)	kinetic Constants ( $\text{min}^{-1}$ )	References
BiOCl/Bi <sub>2</sub> Ti <sub>2</sub> O <sub>7</sub>	Simulated solar light	50	1	0.016	[42]
BiPO <sub>4</sub> Nanorod/Graphene	UV light	20	0.5	0.034	[43]
N-TiO <sub>2</sub> /CNO <sub>NV</sub>	Visible light ( $\lambda > 420 \text{ nm}$ )	30	0.4	0.017	[44]
AgBr-TiO <sub>2</sub> -Pa	Visible light ( $\lambda > 420 \text{ nm}$ )	20	0.5	0.019	[45]
BiOCl@CeO <sub>2</sub>	Visible light ( $\lambda > 420 \text{ nm}$ )	10	0.5	0.015	[46]
Se/BiOCl	Visible light ( $\lambda > 420 \text{ nm}$ )	10	0.5	0.022	[47]
C/BiOCl	Visible light ( $\lambda > 420 \text{ nm}$ )	10	0.5	0.014	[48]
BiOCl	Visible light ( $\lambda > 420 \text{ nm}$ )	10	0.4	0.007	[49]
MWCNTs/Bi <sub>4</sub> O <sub>5</sub> I <sub>2</sub>	Visible light	20	0.2	0.012	[50]
3D-BiOCl	Visible light ( $\lambda > 420 \text{ nm}$ )	30	1	0.025	This work

Stability, in addition to photocatalytic activity, is a critical factor to consider when evaluating a photocatalyst. Recycling studies for TC-HCl photo-degradation under visible light irradiation were carried out to evaluate the photo-stability of 3D-BiOCl, as shown in Figure 4e. As can be observed, there was no discernible decline in photocatalytic activity between each cycle, indicating that the 3D-BiOCl photocatalyst was excellently stable throughout photocatalysis. The unique hierarchical structure of 3D-BiOCl, which results in distinguished settling properties, may be responsible for its excellent stability and recyclability. For further investigation of the active species participating in the photocatalytic process, ammonium oxalate (AO), benzoguinone (BQ), silver nitrate (AgNO<sub>3</sub>), and isopropyl alcohol (IPA) were utilized as holes ( $h^+$ ), superoxide radical anion ( $O_2^-$ ), electrons ( $e^-$ ), and hydroxyl radical ( $\cdot OH$ ) radical scavengers, respectively. With the addition of  $e^-$  and  $\cdot OH$  scavengers, the degradation activity of TC-HCl by 3D-BiOCl does not appear to differ significantly, suggesting that  $e^-$  and  $\cdot OH$  are not the primary radicals in the catalytic process, as shown in Figure 4f. In contrast, when scavengers of  $\cdot O_2^-$  and  $h^+$  were added to the reaction system, TC-HCl degradation behavior was severely suppressed, with only 16 and 68 degradation rate percentages of the control condition, respectively, indicat-

ing that radicals of  $\bullet\text{O}_2^-$  and  $\text{h}^+$ , particularly  $\bullet\text{O}_2^-$ , are essential for visible-light-driven TC-HCl degradation.

To provide insight into the underlying reasons for the superior photocatalytic activity of the target specimens, UV/Vis absorption, photoluminescence (PL), and photo-electrochemical characteristics of BiOCl and 3D-BiOCl were investigated. Generally, lattice defects in semiconductor material would result in changes in the energy band structure, so as to alter the light absorption capabilities of material [15,51,52]. To this end, UV/Vis diffuse reflectance spectra were first performed to investigate the optical absorption properties of BiOCl and 3D-BiOCl. As demonstrated in Figure 5a, 3D-BiOCl exhibits a slightly larger optical absorption edge of 374 nm than BiOCl, which is 365 nm. Moreover, the bandgap energies of the BiOCl samples were further calculated by plotting  $(\alpha h\nu)^{1/2}$  versus photon energy ( $h\nu$ ), as shown in Figure S4. According to the intercepts of the tangent to the x-axis, the  $E_g$  values of BiOCl and 3D-BiOCl were roughly 3.25 and 3.11 eV, respectively [53]. Nevertheless, 3D-BiOCl is still incapable of absorbing energy from visible light, implying that the tiny band gap change is not responsible for the excellent photocatalytic activity of 3D-BiOCl under visible and natural white LED light. It is noteworthy that, unlike pristine BiOCl, 3D-BiOCl exhibits continuous absorption throughout the entire light spectrum, which may stem from the oxygen-vacancy-induced defect states in the forbidden band. As shown in the inset of Figure 5a, such a feature in the energy band results in a significant color shift in the material, intensifying the visible-light-induced photocatalytic activity of 3D-BiOCl [54]. Following the analysis of UV/Vis absorbance, the charge transfer and recombination behaviors were assessed using electrochemical impedance spectra (EIS) and PL emission spectra, respectively, as illustrated in Figure 5b,c. The EIS Nyquist diagrams of 3D-BiOCl, as revealed in Figure 5b, have a smaller curvature radius than BiOCl, showing that the defective hierarchical structure lowers the charge transfer resistance of 3D-BiOCl [55–57]. Furthermore, the fluorescence intensity of 3D-BiOCl in the 350–550 nm bands is substantially weakened compared with that of BiOCl, as seen in Figure 5c. In general, the PL intensity is dictated by the recombination rate of photo-generated carriers; a weak PL intensity suggests a low recombination rate, implying that the hierarchical structure of 3D-BiOCl facilitates the transit of photo-generated carriers, so as to effectively suppress photo-generated charge recombination [58–60]. It is generally believed that strong light absorption, high carrier transfer efficiency, and low carrier recombination would result in high photo-generated carrier concentrations in a sample [61,62]. To corroborate this argument, using a typical three-electrode cell, we have compared the transient photocurrent responses of the acquired samples over three on/off cycles. Both BiOCl and 3D-BiOCl exhibit a swift response when the light is switched on or off, as shown in Figure 5d, and do not display an apparent decrease in current density between cycles, showing continuous and sustainable production of the photo-generated carriers by samples. In addition, as expected, under the identical testing conditions, 3D-BiOCl is characterized by higher photocurrent intensities than pure BiOCl. This means that 3D-BiOCl can create more carriers during the photocatalytic process, thus making it a more active photocatalyst than BiOCl.

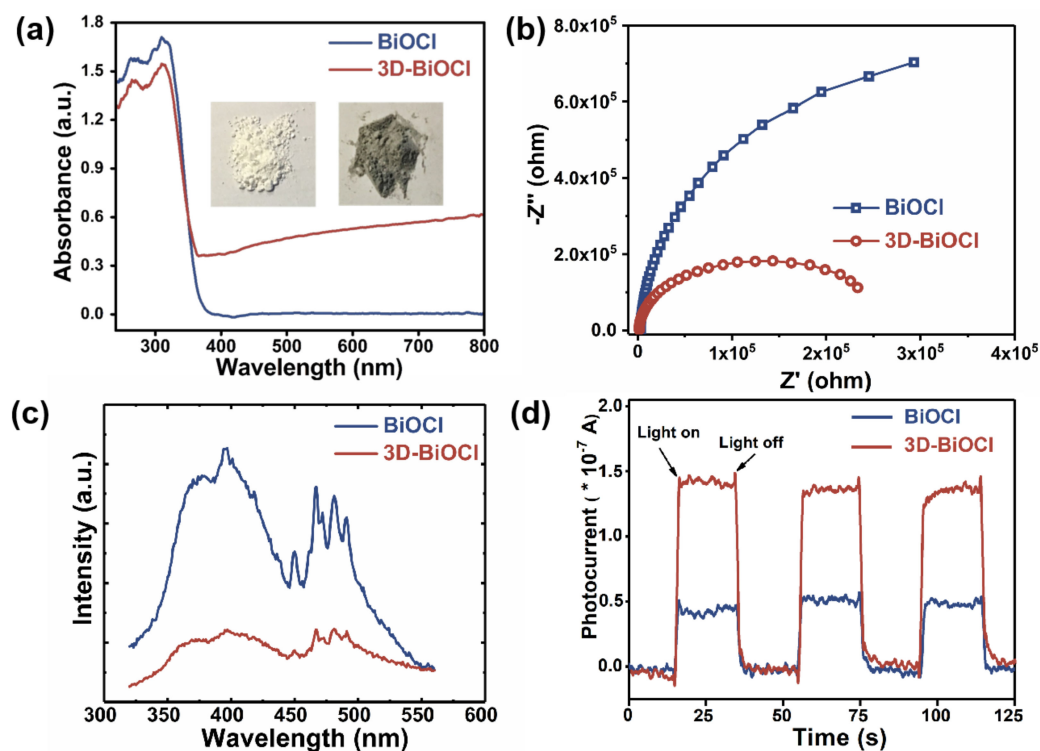


**Figure 5.** (a) UV/Vis absorption, (b) electrochemical impedance spectra, (c) photoluminescence, and (d) transient photocurrent spectra of as-prepared BiOCl photocatalysts.

#### 4. Conclusions

In this study, we developed a method for fabricating 3D hierarchical defective BiOCl at ambient pressure through etching-recrystallization with boiling EG as a treatment solution. The results indicate that the 3D-BiOCl photocatalyst not only possesses a hexagonal prism-like morphology at micron scale that arises from the assembly of BiOCl nanosheets, but also contains abundant oxygen vacancies, validated by SEM, XRD, Raman, and EPR analyses. In accordance with BET, UV/Vis absorbance, and photo-electro-chemical results, 3D-BiOCl was endowed with a higher specific surface area, better light harvesting capabilities, and more efficient separation and transfer of photo-excited charges compared with pristine BiOCl. As a result, 3D-BiOCl presents a remarkable photocatalytic activity for TC-HCl degradation in both visible light and natural white LED light. Furthermore, the target photocatalyst demonstrated an extraordinary recycling potential thanks to its hierarchical structure. In light of its simple and low-energy requirements preparation procedure, high efficiency in pollutants' degradation, and ease of recycling properties, we believe 3D-BiOCl has a promising future in a variety of fields, including decoration materials and wastewater treatment.

**Supplementary Materials:** The following supporting information can be downloaded at: <https://www.mdpi.com/article/10.3390/nano12152700/s1>, Figure S1. UV-Vis spectrum of TC-HCl; Figure S2. SEM picture of BiOCl.; Figure S3. SEM pictures of 3D-BiOCl.; Figure S4. Plots of  $(\alpha h\nu)^{-1/2}$  versus photon energy ( $h\nu$ ) for BiOCl (blue) and 3D-BiOCl (red).

**Author Contributions:** Conceptualization, L.H. and H.W.; methodology, Z.D. and F.Y.; validation, L.H.; formal analysis, Z.D., F.Y., K.L., L.F. and L.H.; investigation, L.F.; resources, H.W.; data curation, L.H. and Z.D.; writing—original draft preparation, Z.D.; writing—review and editing, L.H. and H.W.; visualization, L.H.; supervision, L.H. and H.W.; funding acquisition, L.H. All authors have read and agreed to the published version of the manuscript.

**Funding:** This research was funded by the research grants from the Natural Science Foundation of Hunan (2021JJ40450), the Key Projects of Education Department of Hunan Province, China (20A420), and the Doctoral Scientific Research Foundation of University of South China (190XQD105).

**Institutional Review Board Statement:** Not applicable.

**Informed Consent Statement:** Not applicable.

**Data Availability Statement:** The data presented in this study are available on request from the corresponding authors.

**Acknowledgments:** This work was financially supported by research grants from the Natural Science Foundation of Hunan (2021JJ40450), the Key Projects of Education Department of Hunan Province, China (20A420), and the Doctoral Scientific Research Foundation of University of South China (190XQD105).

**Conflicts of Interest:** The authors declare that they have no known competing financial interests or personal relationships that could have appeared to influence the work reported in this paper.

## References

1. Duan, X.; Zhou, X.; Wang, R.; Wang, S.; Ren, N.-Q.; Ho, S.-H. Advanced oxidation processes for water disinfection: Features, mechanisms and prospects. *Chem. Eng. J.* **2021**, *409*, 128207.
2. Zhang, L.; Lu, W.; Xu, P.; Wang, H.; Wei, X.; Yao, K.; Peng, S. Plasmon-mediated activation of persulfate for efficient photodegradation of ionic liquids over Ag@Pd core-shell nanocubes. *Appl. Catal. B Environ.* **2022**, *301*, 120751. [[CrossRef](#)]
3. Zhang, J.; Jing, B.; Tang, Z.; Ao, Z.; Xia, D.; Zhu, M.; Wang, S. Experimental and DFT insights into the visible-light driving metal-free C<sub>3</sub>N<sub>5</sub> activated persulfate system for efficient water purification. *Appl. Catal. B Environ.* **2021**, *289*, 120023. [[CrossRef](#)]
4. Lee, B.-H.; Gong, E.; Kim, M.; Park, S.; Kim, H.R.; Lee, J.; Jung, E.; Lee, C.W.; Bok, J.; Jung, Y. Electronic interaction between transition metal single-atoms and anatase TiO<sub>2</sub> boosts CO<sub>2</sub> photoreduction with H<sub>2</sub>O. *Energy Environ. Sci.* **2022**, *15*, 601–609. [[CrossRef](#)]
5. Song, S.; Song, H.; Li, L.; Wang, S.; Chu, W.; Peng, K.; Meng, X.; Wang, Q.; Deng, B.; Liu, Q. A selective Au-ZnO/TiO<sub>2</sub> hybrid photocatalyst for oxidative coupling of methane to ethane with dioxygen. *Nat. Catal.* **2021**, *4*, 1032–1042. [[CrossRef](#)]
6. Cheng, L.; Yue, X.; Fan, J.; Xiang, Q. Site-Specific Electron-Driving Observations of CO<sub>2</sub>-to-CH<sub>4</sub> Photoreduction on Co-doped CeO<sub>2</sub>/Crystalline Carbon Nitride S-scheme Heterojunctions. *Adv. Mater.* **2022**, *34*, 2200929. [[CrossRef](#)]
7. Cheng, C.; He, B.; Fan, J.; Cheng, B.; Cao, S.; Yu, J. An Inorganic/Organic S-Scheme Heterojunction H<sub>2</sub>-Production Photocatalyst and its Charge Transfer Mechanism. *Adv. Mater.* **2021**, *33*, 2100317. [[CrossRef](#)]
8. Yang, N.; Zhao, Y.; Wu, P.; Liu, G.; Sun, F.; Ma, J.; Jiang, Z.; Sun, Y.; Zeng, G. Defective C<sub>3</sub>N<sub>4</sub> frameworks coordinated diatomic copper catalyst: Towards mild oxidation of methane to C1 oxygenates. *Appl. Catal. B Environ.* **2021**, *299*, 120682. [[CrossRef](#)]
9. Zhao, X.; Xia, Y.; Li, H.; Wang, X.; Wei, J.; Jiao, X.; Chen, D. Oxygen vacancy dependent photocatalytic CO<sub>2</sub> reduction activity in liquid-exfoliated atomically thin BiOCl nanosheets. *Appl. Catal. B Environ.* **2021**, *297*, 120426. [[CrossRef](#)]
10. Liu, C.; Gao, X.; Zhang, C.; Cheng, T.; Wang, Y.; Zhang, B.; Dong, P.; Chen, X.; Xi, X.; Zou, Z. Layered BiOCl/H<sup>+</sup> TiNbO<sub>5</sub> heterojunctions for boosting visible-light-driven photocatalytic RhB degradation. *Sustain. Energy Fuels* **2021**, *5*, 4680–4689. [[CrossRef](#)]
11. Qi, S.; Liu, X.; Ma, N.; Xu, H. Construction and photocatalytic properties of WS<sub>2</sub>/MoS<sub>2</sub>/BiOCl heterojunction. *Chem. Phys. Lett.* **2021**, *763*, 138203. [[CrossRef](#)]
12. Liu, G.; Wang, B.; Zhu, X.; Ding, P.; Zhao, J.; Li, H.; Chen, Z.; Zhu, W.; Xia, J. Edge-Site-Rich Ordered Macroporous BiOCl Triggers C=O Activation for Efficient CO<sub>2</sub> Photoreduction. *Small* **2022**, *18*, 2105228. [[CrossRef](#)] [[PubMed](#)]
13. Li, H.; Li, J.; Ai, Z.; Jia, F.; Zhang, L. Oxygen vacancy-mediated photocatalysis of BiOCl: Reactivity, selectivity, and perspectives. *Angew. Chem. Int. Ed.* **2018**, *57*, 122–138. [[CrossRef](#)] [[PubMed](#)]
14. Wang, Y.; Batmunkh, M.; Mao, H.; Li, H.; Jia, B.; Wu, S.; Liu, D.; Song, X.; Sun, Y.; Ma, T. Low-overpotential electrochemical ammonia synthesis using BiOCl-modified 2D titanium carbide MXene. *Chin. Chem. Lett.* **2022**, *33*, 394–398. [[CrossRef](#)]
15. Wei, S.; Zhong, H.; Wang, H.; Song, Y.; Jia, C.; Anpo, M.; Wu, L. Oxygen vacancy enhanced visible light photocatalytic selective oxidation of benzylamine over ultrathin Pd/BiOCl nanosheets. *Appl. Catal. B Environ.* **2022**, *305*, 121032. [[CrossRef](#)]
16. Kumar, A.; Kumar, A.; Sharma, G.; Ala'a, H.; Naushad, M.; Ghfar, A.A.; Stadler, F.J. Quaternary magnetic BiOCl/g-C<sub>3</sub>N<sub>4</sub>/Cu<sub>2</sub>O/Fe<sub>3</sub>O<sub>4</sub> nano-junction for visible light and solar powered degradation of sulfamethoxazole from aqueous environment. *Chem. Eng. J.* **2018**, *334*, 462–478. [[CrossRef](#)]
17. Shi, Y.; Zhan, G.; Li, H.; Wang, X.; Liu, X.; Shi, L.; Wei, K.; Ling, C.; Li, Z.; Wang, H. Simultaneous manipulation of bulk excitons and surface defects for ultrastable and highly selective CO<sub>2</sub> photoreduction. *Adv. Mater.* **2021**, *33*, 2100143. [[CrossRef](#)]
18. Liu, J.; Li, D.; Li, R.; Wang, Y.; Wang, Y.; Fan, C. PtO/Pt<sup>4+</sup>-BiOCl with enhanced photocatalytic activity: Insight into the defect-filled mechanism. *Chem. Eng. J.* **2020**, *395*, 123954. [[CrossRef](#)]
19. Li, Y.L.; Liu, Y.; Mu, H.Y.; Liu, R.H.; Hao, Y.J.; Wang, X.J.; Hildebrandt, D.; Liu, X.; Li, F.T. The simultaneous adsorption, activation and in situ reduction of carbon dioxide over Au-loading BiOCl with rich oxygen vacancies. *Nanoscale* **2021**, *13*, 2585–2592. [[CrossRef](#)]
20. Tian, C.; Luo, S.; She, J.; Qing, Y.; Yan, N.; Wu, Y.; Liu, Z. Cellulose nanofibrils enable flower-like BiOCl for high-performance photocatalysis under visible-light irradiation. *Appl. Surf. Sci.* **2019**, *464*, 606–615. [[CrossRef](#)]

21. Lin, E.; Huang, R.; Wu, J.; Kang, Z.; Ke, K.; Qin, N.; Bao, D. Recyclable CoFe<sub>2</sub>O<sub>4</sub> modified BiOCl hierarchical microspheres utilizing photo, photothermal and mechanical energy for organic pollutant degradation. *Nano Energy* **2021**, *89*, 106403. [[CrossRef](#)]
22. Chen, S.; Huang, D.; Xu, P.; Xue, W.; Lei, L.; Chen, Y.; Zhou, C.; Deng, R.; Wang, W. Topological transformation of bismuth vanadate into bismuth oxychloride: Band-gap engineering of ultrathin nanosheets with oxygen vacancies for efficient molecular oxygen activation. *Chem. Eng. J.* **2021**, *420*, 127573. [[CrossRef](#)]
23. Zhang, B.; Zhang, J.; Duan, R.; Wan, Q.; Tan, X.; Su, Z.; Han, B.; Zheng, L.; Mo, G. BiOCl nanosheets with periodic nanochannels for high-efficiency photooxidation. *Nano Energy* **2020**, *78*, 105340. [[CrossRef](#)]
24. Cui, D.; Wang, L.; Xu, K.; Ren, L.; Wang, L.; Yu, Y.; Du, Y.; Hao, W. Band-gap engineering of BiOCl with oxygen vacancies for efficient photooxidation properties under visible-light irradiation. *J. Mater. Chem. A* **2018**, *6*, 2193–2199. [[CrossRef](#)]
25. Qin, H.; Sun, J.; Xia, D.; Xu, H.; Yu, Q.; Zheng, Y.; Shi, Y. Boosting nonradical process in BiOI/BiOCl heterostructure by interface oxygen vacancies. *Chem. Eng. J.* **2022**, *435*, 134847. [[CrossRef](#)]
26. Cui, D.; Xu, K.; Dong, X.; Lv, D.; Dong, F.; Hao, W.; Du, Y.; Chen, J. Controlled hydrogenation into defective interlayer bismuth oxychloride via vacancy engineering. *Commun. Chem.* **2020**, *3*, 73. [[CrossRef](#)]
27. Zhang, X.-H.; Guo, R.-C.; Chen, Y.-F.; Xu, X.; Yang, Z.-X.; Cheng, D.-B.; Chen, H.; Qiao, Z.-Y.; Wang, H. A BiOCl nanodevice for pancreatic tumor imaging and mitochondria-targeted therapy. *Nano Today* **2021**, *40*, 101285. [[CrossRef](#)]
28. Li, H.; Chen, S.; Shang, H.; Wang, X.; Yang, Z.; Ai, Z.; Zhang, L. Surface hydrogen bond network spatially confined BiOCl oxygen vacancy for photocatalysis. *Sci. Bull.* **2020**, *65*, 1916–1923. [[CrossRef](#)]
29. Xiong, J.; Cheng, G.; Li, G.; Qin, F.; Chen, R. Well-crystallized square-like 2D BiOCl nanoplates: Mannitol-assisted hydrothermal synthesis and improved visible-light-driven photocatalytic performance. *RSC Adv.* **2011**, *1*, 1542–1553.
30. Mi, Y.; Wen, L.; Wang, Z.; Cao, D.; Fang, Y.; Lei, Y. Building of anti-restack 3D BiOCl hierarchitectures by ultrathin nanosheets towards enhanced photocatalytic activity. *Appl. Catal. B Environ.* **2015**, *176–177*, 331–337. [[CrossRef](#)]
31. Su, Q.; Zhu, L.; Zhang, M.; Li, Y.; Liu, S.; Lin, J.; Song, F.; Zhang, W.; Zhu, S.; Pan, J. Construction of a bioinspired hierarchical BiVO<sub>4</sub>/BiOCl heterojunction and its enhanced photocatalytic activity for phenol degradation. *ACS Appl. Mater. Interfaces* **2021**, *13*, 32906–32915. [[CrossRef](#)] [[PubMed](#)]
32. Sun, J.; Wu, S.; Yang, S.-Z.; Li, Q.; Xiong, J.; Yang, Z.; Gu, L.; Zhang, X.; Sun, L. Enhanced photocatalytic activity induced by sp<sup>3</sup> to sp<sup>2</sup> transition of carbon dopants in BiOCl crystals. *Appl. Catal. B Environ.* **2018**, *221*, 467–472. [[CrossRef](#)]
33. Gong, S.; Rao, F.; Zhang, W.; Hassan, Q.-U.; Liu, Z.; Gao, J.; Lu, J.; Hojamberdiev, M.; Zhu, G. Au nanoparticles loaded on hollow BiOCl microstructures boosting CO<sub>2</sub> photoreduction. *Chin. Chem. Lett.* **2021**, *33*, 4385–4388. [[CrossRef](#)]
34. Kuila, A.; Saravanan, P.; Bahnemann, D.; Wang, C. Novel Ag decorated, BiOCl surface doped AgVO<sub>3</sub> nanobelt ternary composite with Z-scheme homojunction-heterojunction interface for high prolific photo switching, quantum efficiency and hole mediated photocatalysis. *Appl. Catal. B Environ.* **2021**, *293*, 120224. [[CrossRef](#)]
35. Cao, J.; Cen, W.; Jing, Y.; Du, Z.; Chu, W.; Li, J. P-doped BiOCl for visible light photodegradation of tetracycline: An insight from experiment and calculation. *Chem. Eng. J.* **2022**, *435*, 134683. [[CrossRef](#)]
36. Ansari, S.A.; Khan, M.M.; Kalathil, S.; Nisar, A.; Lee, J.; Cho, M.H. Oxygen vacancy induced band gap narrowing of ZnO nanostructures by an electrochemically active biofilm. *Nanoscale* **2013**, *5*, 9238–9246. [[CrossRef](#)] [[PubMed](#)]
37. Deng, F.; Zhang, Q.; Yang, L.; Luo, X.; Wang, A.; Luo, S.; Dionysiou, D.D. Visible-light-responsive graphene-functionalized Bi-bridge Z-scheme black BiOCl/Bi<sub>2</sub>O<sub>3</sub> heterojunction with oxygen vacancy and multiple charge transfer channels for efficient photocatalytic degradation of 2-nitrophenol and industrial wastewater treatment. *Appl. Catal. B Environ.* **2018**, *238*, 61–69. [[CrossRef](#)]
38. Wang, L.; Lv, D.; Dong, F.; Wu, X.; Cheng, N.; Scott, J.; Xu, X.; Hao, W.; Du, Y. Boosting visible-light-driven photo-oxidation of BiOCl by promoted charge separation via vacancy engineering. *ACS Sustain. Chem. Eng.* **2019**, *7*, 3010–3017. [[CrossRef](#)]
39. Yan, Z.; Dai, Z.; Zheng, W.; Lei, Z.; Qiu, J.; Kuang, W.; Huang, W.; Feng, C. Facile ammonium oxidation to nitrogen gas in acid wastewater by in situ photogenerated chlorine radicals. *Water Res.* **2021**, *205*, 117678. [[CrossRef](#)]
40. Zhang, L.; Wang, W.; Jiang, D.; Gao, E.; Sun, S. Photoreduction of CO<sub>2</sub> on BiOCl nanoplates with the assistance of photoinduced oxygen vacancies. *Nano Res.* **2015**, *8*, 821–831. [[CrossRef](#)]
41. Zhang, L.; Han, Z.; Wang, W.; Li, X.; Su, Y.; Jiang, D.; Lei, X.; Sun, S. Solar-light-driven pure water splitting with ultrathin BiOCl nanosheets. *Chem. Eur. J.* **2015**, *21*, 18089–18094. [[CrossRef](#)] [[PubMed](#)]
42. Xu, Y.; Lin, D.; Liu, X.; Luo, Y.; Xue, H.; Huang, B.; Chen, Q.; Qian, Q. Electrospun BiOCl/Bi<sub>2</sub>Ti<sub>2</sub>O<sub>7</sub> nanorod heterostructures with enhanced solar light efficiency in the photocatalytic degradation of tetracycline hydrochloride. *ChemCatChem* **2018**, *10*, 2496–2504. [[CrossRef](#)]
43. Wang, Y.; Qiang, Z.; Zhu, W.; Yao, W.; Tang, S.; Yang, Z.; Wang, J.; Duan, J.; Ma, C.; Tan, R. BiPO<sub>4</sub> nanorod/graphene composite heterojunctions for photocatalytic degradation of tetracycline hydrochloride. *ACS Appl. Nano Mater.* **2021**, *4*, 8680–8689. [[CrossRef](#)]
44. Wang, Y.; Rao, L.; Wang, P.; Shi, Z.; Zhang, L. Photocatalytic activity of N-TiO<sub>2</sub>/O-doped N vacancy g-C<sub>3</sub>N<sub>4</sub> and the intermediates toxicity evaluation under tetracycline hydrochloride and Cr (VI) coexistence environment. *Appl. Catal. B Environ.* **2020**, *262*, 118308. [[CrossRef](#)]
45. Shi, Y.; Yan, Z.; Xu, Y.; Tian, T.; Zhang, J.; Pang, J.; Peng, X.; Zhang, Q.; Shao, M.; Tan, W. Visible-light-driven AgBr-TiO<sub>2</sub>-Palygorskite photocatalyst with excellent photocatalytic activity for tetracycline hydrochloride. *J. Clean. Prod.* **2020**, *277*, 124021. [[CrossRef](#)]

46. Wang, H.; Liao, B.; Lu, T.; Ai, Y.; Liu, G. Enhanced visible-light photocatalytic degradation of tetracycline by a novel hollow BiOCl@ CeO<sub>2</sub> heterostructured microspheres: Structural characterization and reaction mechanism. *J. Hazard. Mater.* **2020**, *385*, 121552. [[CrossRef](#)]
47. Huang, H.; Ma, C.; Zhu, Z.; Yao, X.; Liu, Y.; Liu, Z.; Li, C.; Yan, Y. Insights into enhanced visible light photocatalytic activity of t-Se nanorods/BiOCl ultrathin nanosheets 1D/2D heterojunctions. *Chem. Eng. J.* **2018**, *338*, 218–229. [[CrossRef](#)]
48. Yan, Y.; Tang, X.; Ma, C.; Huang, H.; Yu, K.; Liu, Y.; Lu, Z.; Li, C.; Zhu, Z.; Huo, P. A 2D mesoporous photocatalyst constructed by the modification of biochar on BiOCl ultrathin nanosheets for enhancing the TC-HCl degradation activity. *New J. Chem.* **2020**, *44*, 79–86. [[CrossRef](#)]
49. Guan, C.; Hou, T.; Nie, W.; Zhang, Q.; Duan, L.; Zhao, X. Facet synergy dominant Z-scheme transition in BiOCl with enhanced 1O<sub>2</sub> generation. *Chemosphere* **2022**, *307*, 135663. [[CrossRef](#)]
50. Gao, P.; Li, Z.; Feng, L.; Liu, Y.; Du, Z.; Zhang, L. Construction of novel MWCNTs/Bi<sub>4</sub>O<sub>5</sub>I<sub>2</sub> nanosheets with enhanced adsorption and photocatalytic performance for the degradation of tetracycline: Efficiency, mechanism and regeneration. *Chem. Eng. J.* **2022**, *429*, 132398. [[CrossRef](#)]
51. Ye, X.; Li, Y.; Luo, P.; He, B.; Cao, X.; Lu, T. Iron sites on defective BiOBr nanosheets: Tailoring the molecular oxygen activation for enhanced photocatalytic organic synthesis. *Nano Res.* **2022**, *15*, 1509–1516. [[CrossRef](#)]
52. Wang, H.; Yang, W.; Bian, K.; Zeng, W.; Jin, X.; Ouyang, R.; Xu, Y.; Dai, C.; Zhou, S.; Zhang, B. Oxygen-Deficient BiOCl Combined with L-Buthionine-Sulfoximine Synergistically Suppresses Tumor Growth through Enhanced Singlet Oxygen Generation under Ultrasound Irradiation. *Small* **2022**, *18*, 2104550. [[CrossRef](#)] [[PubMed](#)]
53. D'amato, C.; Giovannetti, R.; Zannotti, M.; Rommozzi, E.; Ferraro, S.; Seghetti, C.; Minicucci, M.; Gunnella, R.; Di Cicco, A. Enhancement of visible-light photoactivity by polypropylene coated plasmonic Au/TiO<sub>2</sub> for dye degradation in water solution. *Appl. Surf. Sci.* **2018**, *441*, 575–587. [[CrossRef](#)]
54. Qin, Y.; Lu, J.; Zhao, X.; Lin, X.; Hao, Y.; Huo, P.; Meng, M.; Yan, Y. Nitrogen defect engineering and  $\pi$ -conjugation structure decorated g-C<sub>3</sub>N<sub>4</sub> with highly enhanced visible-light photocatalytic hydrogen evolution and mechanism insight. *Chem. Eng. J.* **2021**, *425*, 131844. [[CrossRef](#)]
55. Li, G.; Deng, X.; Chen, P.; Wang, X.; Ma, J.; Liu, F.; Yin, S.-F. Sulphur vacancies-VS<sub>2</sub>@ C<sub>3</sub>N<sub>4</sub> driven by in situ supramolecular self-assembly for synergistic photocatalytic degradation of real wastewater and H<sub>2</sub> production: Vacancies taming interfacial compact heterojunction and carriers transfer. *Chem. Eng. J.* **2022**, *433*, 134505. [[CrossRef](#)]
56. Jang, D.; Choi, S.; Kwon, N.H.; Jang, K.Y.; Lee, S.; Lee, T.-W.; Hwang, S.-J.; Kim, H.; Kim, J.; Park, S. Water-assisted formation of amine-bridged carbon nitride: A structural insight into the photocatalytic performance for H<sub>2</sub> evolution under visible light. *Appl. Catal. B Environ.* **2022**, *310*, 121313. [[CrossRef](#)]
57. Abazari, R.; Mahjoub, A.R.; Salehi, G. Preparation of amine functionalized g-C<sub>3</sub>N<sub>4</sub>@ H/SMOF NCs with visible light photocatalytic characteristic for 4-nitrophenol degradation from aqueous solution. *J. Hazard. Mater.* **2019**, *365*, 921–931. [[CrossRef](#)]
58. Le, S.; Zhu, C.; Cao, Y.; Wang, P.; Liu, Q.; Zhou, H.; Chen, C.; Wang, S.; Duan, X. V<sub>2</sub>O<sub>5</sub> nanodot-decorated laminar C<sub>3</sub>N<sub>4</sub> for sustainable photodegradation of amoxicillin under solar light. *Appl. Catal. B Environ.* **2022**, *303*, 120903. [[CrossRef](#)]
59. Zhou, X.; Liu, Y.; Jin, Z.; Huang, M.; Zhou, F.; Song, J.; Qu, J.; Zeng, Y.J.; Qian, P.C.; Wong, W.Y. Solar-Driven Hydrogen Generation Catalyzed by g-C<sub>3</sub>N<sub>4</sub> with Poly (platinaynes) as Efficient Electron Donor at Low Platinum Content. *Adv. Sci.* **2021**, *8*, 2002465. [[CrossRef](#)]
60. Hu, L.; Li, M.; Yang, K.; Xiong, Z.; Yang, B.; Wang, M.; Tang, X.; Zang, Z.; Liu, X.; Li, B.; et al. PEDOT:PSS monolayers to enhance the hole extraction and stability of perovskite solar cells. *J. Mater. Chem. A* **2018**, *6*, 16583–16589. [[CrossRef](#)]
61. Reddy, C.V.; Koutavarapu, R.; Shim, J.; Cheolho, B.; Reddy, K.R. Novel g-C<sub>3</sub>N<sub>4</sub>/Cu-doped ZrO<sub>2</sub> hybrid heterostructures for efficient photocatalytic Cr (VI) photoreduction and electrochemical energy storage applications. *Chemosphere* **2022**, *295*, 133851. [[CrossRef](#)] [[PubMed](#)]
62. Jia, Y.; Li, S.; Ma, H.; Gao, J.; Zhu, G.; Zhang, F.; Park, J.Y.; Cha, S.; Bae, J.-S.; Liu, C. Oxygen vacancy rich Bi<sub>2</sub>O<sub>4</sub>-Bi<sub>4</sub>O<sub>7</sub>-BiO<sub>2</sub>-x composites for UV-vis-NIR activated high efficient photocatalytic degradation of bisphenol A. *J. Hazard. Mater.* **2020**, *382*, 121121. [[CrossRef](#)] [[PubMed](#)]